

Euler-Lagrange CFD modelling of unconfined gas mixing in anaerobic digestion

Dapelo, Davide; Alberini, Federico; Bridgeman, Jonathan

DOI:

[10.1016/j.watres.2015.08.042](https://doi.org/10.1016/j.watres.2015.08.042)

License:

Creative Commons: Attribution-NonCommercial-NoDerivs (CC BY-NC-ND)

Document Version

Peer reviewed version

Citation for published version (Harvard):

Dapelo, D, Alberini, F & Bridgeman, J 2015, 'Euler-Lagrange CFD modelling of unconfined gas mixing in anaerobic digestion', *Water Research*, vol. 85, pp. 497-511. <https://doi.org/10.1016/j.watres.2015.08.042>

[Link to publication on Research at Birmingham portal](#)

Publisher Rights Statement:

Eligibility for repository: checked 15/10/2015

General rights

Unless a licence is specified above, all rights (including copyright and moral rights) in this document are retained by the authors and/or the copyright holders. The express permission of the copyright holder must be obtained for any use of this material other than for purposes permitted by law.

- Users may freely distribute the URL that is used to identify this publication.
- Users may download and/or print one copy of the publication from the University of Birmingham research portal for the purpose of private study or non-commercial research.
- User may use extracts from the document in line with the concept of 'fair dealing' under the Copyright, Designs and Patents Act 1988 (?)
- Users may not further distribute the material nor use it for the purposes of commercial gain.

Where a licence is displayed above, please note the terms and conditions of the licence govern your use of this document.

When citing, please reference the published version.

Take down policy

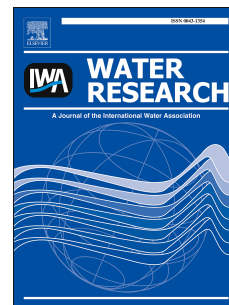
While the University of Birmingham exercises care and attention in making items available there are rare occasions when an item has been uploaded in error or has been deemed to be commercially or otherwise sensitive.

If you believe that this is the case for this document, please contact UBIRA@lists.bham.ac.uk providing details and we will remove access to the work immediately and investigate.

Accepted Manuscript

Euler-Lagrange CFD modelling of unconfined gas mixing in anaerobic digestion

Davide Dapelo, Federico Alberini, John Bridgeman



PII: S0043-1354(15)30193-7

DOI: [10.1016/j.watres.2015.08.042](https://doi.org/10.1016/j.watres.2015.08.042)

Reference: WR 11489

To appear in: *Water Research*

Received Date: 2 April 2015

Revised Date: 13 July 2015

Accepted Date: 22 August 2015

Please cite this article as: Dapelo, D., Alberini, F., Bridgeman, J., Euler-Lagrange CFD modelling of unconfined gas mixing in anaerobic digestion, *Water Research* (2015), doi: 10.1016/j.watres.2015.08.042.

This is a PDF file of an unedited manuscript that has been accepted for publication. As a service to our customers we are providing this early version of the manuscript. The manuscript will undergo copyediting, typesetting, and review of the resulting proof before it is published in its final form. Please note that during the production process errors may be discovered which could affect the content, and all legal disclaimers that apply to the journal pertain.

Euler-Lagrange CFD modelling of unconfined gas mixing in anaerobic digestion

Davide Dapelo^{a,*}, Federico Alberini^b, John Bridgeman^a

^aUniversity of Birmingham, School of Civil Engineering, Birmingham B15 2TT, United Kingdom

^bUniversity of Birmingham, School of Chemical Engineering

Abstract

A novel Euler-Lagrangian (EL) computational fluid dynamics (CFD) finite volume-based model to simulate the gas mixing of sludge for anaerobic digestion is developed and described. Fluid motion is driven by momentum transfer from bubbles to liquid. Model validation is undertaken by assessing the flowfield in a lab-scale model with particle image velocimetry (PIV). Conclusions are drawn about the upscaling and applicability of the model to full-scale problems, and recommendations are given for optimum application.

Keywords: CFD, Euler-Lagrangian, Anaerobic digestion, Non-Newtonian fluid, Gas mixing, PIV

[Table 1 about here.]

1. Introduction

Through the production of biogas, anaerobic digestion is one of the most technically-mature and cost-effective processes for sustainable energy production and management of sludges from livestock facilities, municipal solid waste and wastewater treatment plants.

*Corresponding author.
Tel.: +44 (0) 121 414 5145
Email: dxd265@bham.ac.uk

15 A key component for the success of an anaerobic digestion plant is mixing: proper
16 mixing ensures uniformity of temperature, enables colonies of bacteria to digest the
17 material entering the digester evenly, and prevents the formation of surface crusts.
18 However, mixing is generally an energy intensive operation, with approximately 20%
19 of the total energy input of digesters absorbed by mixing (Bridgeman, 2012). For this
20 reason, mixing should be optimized in order to optimize biogas production. In this
21 sense, optimization seeks the minimum degree of mixing in order to save energy,
22 without compromising, and indeed enhancing, biogas production.

23 Although the importance of thorough mixing has always been recognised, recent
24 studies, both traditional (Stroot et al., 2001; McMahon et al., 2001; Ong et al., 2002;
25 Gómez et al., 2006; Ward et al., 2008) and CFD-based (Bridgeman, 2012; Wu, 2012),
26 point out that an excess of mixing can have a detrimental effect both on the
27 economics of an anaerobic digestion plant and on the process of digestion itself.

28 The two main mixing methods are: mechanical mixing and gas mixing. The former
29 employs impellers to stir the sludge; whereas in the latter, biogas is taken from the
30 top of the tank and pumped into the sludge through a series of nozzles. The bubbles
31 rise in columns via buoyancy and transfer momentum to the surrounding sludge. This
32 momentum transfer takes place due to the push force that the bubbles exert to the
33 surrounding liquid, and the riptide effect arising from the low-pressure region created
34 by the motion of the bubbles.

35 Thanks to the progress of computer performance, computational fluid dynamics
36 (CFD) has become an invaluable resource in the simulation of processes involving
37 fluid flow and heat transfer. However, while a lot of work has been done to
38 understand mechanical mixing of sludge in anaerobic digestion, gas mixing still
39 remains poorly studied. During the gas-mixing process, a complex pattern of
40 momentum exchange between bubbles and liquid phase takes place, and therefore a

genuine multiphase model is required to reproduce the liquid phase mixing robustly and with fidelity. However, to our knowledge, only Vesvikar and Al-Dahhan (2005); Wu (2010, 2012) have investigated this subject with a robust multiphase model. Karim et al. (2007) investigated gas mixing, but they carried out broad simplifications in their analysis, as their model works only on a specific case of draft tube-driven mixing. Furthermore, the effect of gas injection was modelled by specifying the outlet velocity at the exit of the draft tube, while the inside the draft tube were not studied. As can be seen, their analysis was actually carried out with a single-phase model: even though their model was able to reproduce the experimental data satisfactorily, it was specific for a very definite problem. Vesvikar and Al-Dahhan (2005) investigated gas mixing in a lab-scale digester with a Euler-Euler two-way-coupling model; Wu (2010, 2012) performed extensive studies by expanding this model to non-Newtonian liquid phases, by comparing the outcome of the model for a broad set of turbulent models, and by integrating the fluid dynamics with a biochemical model. There is not a universal multiphase model that is optimal to every application (Andersson et al., 2012) – different approaches are possible, each with specific advantages and disadvantages. The Euler-Euler model can handle very complex flows, and this is one of the reasons why it has been largely employed. However, a quantity of empirical information is needed in order to close the momentum equations (Andersson et al., 2012), whereas the Euler-Lagrange model requires a much smaller amount of modelling for closure. For this reason, if the particle number is not too high and the computational expense remains acceptable, the Euler-Lagrangian model provides an attractive alternative. However, no Euler-Lagrange finite volume-based model has been proposed in the literature to simulate gas mixing in anaerobic digestion. Sungkorn et al. (2011) studied highly turbulent constant-viscosity column bubbly flow, while Sungkorn et al. (2012) modelled a generic shear-thinning aerated

67 stirred tank. However, they did not attempt to reproduce the rheologic characteristics
 68 of sludge and, most significantly, they adopted a Lattice-Boltzmann scheme, that is a
 69 completely different framework from finite volume. In the finite volume scheme, the
 70 fluid is modelled as a continuum, and the aim is to solve the Navier-Stokes equations
 71 for the Eulerian velocity $\mathbf{u}(\mathbf{x}, t)$ and pressure $p(\mathbf{x}, t)$ fields. The discretization is
 72 carried out by dividing the domain into cells and defining the velocity and pressure
 73 fields at the centre of each cell. The Navier-Stokes equations are discretized by
 74 applying the Gauss theorem at each cell, and using different discretization schemes in
 75 order to interpolate the values of the fields at the cell borders. The numerical solution
 76 is carried out with an iterative procedure that solves in turn the momentum
 77 Navier-Stokes equation and a Poisson equation for the pressure derived from the
 78 Navier-Stokes and the mass conservation equations, using the solution of one as a
 79 starting guess for the others until convergence is achieved. In the Lattice-Boltzmann
 80 scheme, the fluid is modelled as an ensemble of particles to be treated statistically,
 81 and is described by the probability density function $f(\mathbf{x}, \mathbf{v}, t)$ of finding a particle of
 82 velocity comprised between \mathbf{v} and $\mathbf{v} + d\mathbf{v}$ inside the volume element $(\mathbf{x}, \mathbf{x} + d\mathbf{x})$ and
 83 the time interval $(t, t + dt)$. The probability density function obeys the Boltzmann
 84 equation, which relates its total derivative with a collision operator. Density, velocity
 85 and pressure fields are worked out from the probability density function. The
 86 discretization is carried out by defining a lattice in which the grid points are linked
 87 with unitary velocity vectors. The probability density function is defined at the grid
 88 points. Each grid point is linked to its neighbours via velocity direction vectors. In
 89 order to obtain a physically meaningful solution, it is crucial to define a grid with a
 90 sufficiently rich symmetry group. For each lattice velocity direction, the corresponding
 91 probability density function is obtained by evolving it from the previous timestep by
 92 using the Boltzmann equation according with the scattering matrix and the deviation

93 of the probability density function from the Maxwell (equilibrium) function. The
 94 interested reader can consult literature on finite volume CFD such as Versteeg and
 95 Malalasekera 1995; Andersson et al. 2012 and on lattice-Boltzmann Succi 2001;
 96 Wolf-Gladrow 2005.
 97 The aim of the work reported in this paper is to propose, develop and validate the
 98 first Euler-Lagrange finite volume-based model for investigating gas mixing in
 99 anaerobic digestion. Sungkorn et al. (2011, 2012) formulated the hypothesis that the
 100 requirement for Euler-Lagrangian models of minimum mesh to bubble size ratio (van
 101 Wachem and Almstedt, 2003; Andersson et al., 2012) could be relaxed, and validated
 102 it inside the Lattice-Boltzmann framework; in the work reported in this paper, this
 103 hypothesis was tested in the finite volume framework. Model validation was
 104 performed by comparing model outputs with PIV measurements conducted on a 4
 105 litre laboratory-scale tank. Once the validation has been carried out, it will be
 106 possible to apply the model to full-scale modelling in future works. The full-scaling
 107 will be expected to be less sensitive than the laboratory-scale application proposed in
 108 this work because the mesh size in the former will be expected to be increased and,
 109 consequently, the mesh to bubble size ratio will increase as well, thus respecting the
 110 requirement stated by van Wachem and Almstedt (2003); Andersson et al. (2012).

111 **2. Material and Methods**

112 *2.1. Experimental rig*

113 A 4-litre cylindrical, transparent tank was assembled by gluing a 20 cm diameter, 20
 114 cm long, 3 mm thick plexiglass pipe onto a square support of side 25.5 cm. Care was
 115 taken in order to make sure that the plexiglass pipe axis passed through the support
 116 centre. The junction was sealed with silicon.

117 In order to minimize the refraction of the PIV laser beam through the curved

plexiglass surface, the cylindrical tank was encased within a plexiglass tank fixed to the square support which was subsequently filled with water. The glass layer was set orthogonal to the PIV camera such that refraction through the water-glass and glass-air interfaces might be neglected.

A simple nozzle arrangement was effected by drilling a 1 mm diameter hole through the axis of a plastic bolt of 10 mm head diameter, 5 mm internal diameter, 25 mm length. A hole with the same diameter of the bolt and a compatible threading was drilled at the centre of the squared support. The bolt was screwed through it such that its head remained at the inner side of the support. The bolt head was neglected in the simulations as its size is negligible if compared with the plexiglass pipe. A sketch of the tank is depicted in Figure 1.

[Figure 1 about here.]

The air flow was generated by a Nitto Kohki Co., LTD LA-28B air compressor and flow rate was controlled between 0 and 65 ml s⁻¹ using a Cole-Parmer EW-03216-14 correlated flowmeter with valve. Flexible plastic 5 mm diameter PVC pipes connected the pump to the flowmeter and the flowmeter to the bolt at the back of the square support.

2.2. Fluid Rheology

The stress tensor τ is defined in terms of the shear rate tensor $\dot{\gamma}$ and the dynamic viscosity μ :

$$\tau_{ij} = \mu \dot{\gamma}_{ij} . \quad (1)$$

The shear rate $\dot{\gamma}$ is defined in terms of derivatives of the Eulerian velocity field \mathbf{u} :

$$\dot{\gamma}_{ij} = \partial_i u_j + \partial_j u_i . \quad (2)$$

141 Sludge rheology is complex. It displays non-Newtonian characteristics such as shear
 142 thinning, yield stress and shear banding (Baudez et al., 2013). Moreover, it often
 143 contains sand, cellulosic fibres and other debris, and therefore can be subject to
 144 sedimentation. However, the first approximation of considering the sludge as a
 145 power-law fluid with no sedimentation occurring proved to work well in a broad set of
 146 literature (e.g., Terashima et al. 2009; Bridgeman 2012; Wu 2014). In a power-law
 147 fluid the viscosity is not a constant, but depends on the shear rate magnitude $|\dot{\gamma}|$:

$$148 \quad \mu = K |\dot{\gamma}|^{n-1}, \quad (3)$$

149 where K is the consistency coefficient (Pa s^n) and n is the power law index. In the
 150 case of the sludge we have $n < 1$, that is a pseudoplastic fluid. Here $|\dot{\gamma}|$ is defined as
 151 follows:

$$152 \quad |\dot{\gamma}| = \frac{1}{\sqrt{2}} \sqrt{\dot{\gamma}_{ij} \dot{\gamma}_{ij}}. \quad (4)$$

153 Equation 3 holds only for an interval $(|\dot{\gamma}|_{\min}, |\dot{\gamma}|_{\max})$ (Wu and Chen, 2008;
 154 Bridgeman, 2012). Beyond that interval, the viscosity takes a constant maximum or
 155 minimum value. The values of μ_{\min} and μ_{\max} do not have physical meaning and are
 156 necessary to avoid singular values for the viscosity during the runs as well as to avoid
 157 unnecessary iterations. These values were chosen in a way that the maximum and
 158 minimum viscosity are comprised inside the interval $(|\dot{\gamma}|_{\min}, |\dot{\gamma}|_{\max})$ once stationary
 159 conditions had been reached. During the simulation runs, the value of μ is evaluated
 160 from Equation 2, Equation 4 according to the limitations on $|\dot{\gamma}|$ described above, and
 161 Equation 3, for every point \mathbf{r} and time t . The field $\mu(\mathbf{r}, t)$ thus obtained is used as an
 162 input to compute the velocity field.

163 Achkari-Begdouri and Goodrich (1992) investigated dairy cattle manure, and stated
 164 that the rheologic characteristics of the sludge depend on the total solid ratio (TS)

and the temperature. Wu and Chen (2008) used their data as a basis for modelling sludge. These data are reported in Table 1 where the sludge densities for different TS are shown. All the values of density differ by less than 1% from water density at 35 degrees (994 kg/m³). For the sake of simplicity, in the CFD simulations a constant density of 1,000 kg m⁻³ was assumed.

[Table 2 about here.]

2.3. Preparation of the Liquid Phase

In the work reported here, water solutions of Sigma-Aldrich 419338 sodium carboxymethyl cellulose (CMC) with average molar weight of 700,000 were used in order to reproduce the behaviour of sludge. CMC is polymeric cellulose derivative that is widely used for reproducing pseudoplastic fluids, and, in particular, sludges (e.g. Wu and Chen (2008)). It consists of a white powder that can be dissolved into water and gives rise to a transparent solution. Three CMC solutions were employed, namely 2, 4 and 8 g l⁻¹. Each solution was prepared in the following way. (i) 5 litres of room temperature, tap water were poured into a bucket. (ii) A 20 cm width, 4 cm height rectangular impeller was used to stir the water. The impeller angular velocity was set in order to guarantee a sufficient degree of mixing, but to minimise the inclusion of air bubbles into the water. (iii) The CMC powder was added to the water at a rate not greater than 5 g min⁻¹. (iv) The impeller mixed the solutions for between one and two hours, whereupon it was removed and the bucket sealed. The solution was left standing at room temperature for at least 24 hours. Once filled with the CMC solutions, the wet height of the tank was 13 cm.

2.4. Rheological Measurements

Sludge rheology was assessed using a TA Instruments AR1000 rheometer fitted with a 40 mm diameter 2° steel cone.

Viscosity measurements were performed in the shear rate interval 100—500 s⁻¹ and fitted to the power-law relation of Equation 3. The results are shown in Figure 2, and rheological data are reported in Table 2. The power-law assumption is clearly verified.

[Figure 2 about here.]

[Table 3 about here.]

2.5. Particle Image Velocimetry and High Speed Camera

PIV measurements were performed using a TSI PIV system (TSI Inc, USA). The system comprised a 532 nm (green) Nd-Yag laser (New Wave Solo III) pulsing at 7 Hz, synchronized to a single TSI Power view 4MP (2048 x 2048 pixels) 12 bit CCD camera using a synchronizer (TSI 610035) attached to a personal computer. The PIV system was controlled using TSI Insight 4G software. The spatial resolution of the measurements was 977 $\mu\text{m pixel}^{-1}$. Insight software was used to process the sets of pair raw images and convert them in a $n \times 4$ matrix, where n is the number of cell of the grid and the four columns are x position, y position, x velocity and y velocity. Each experiment captured 300 images which were used to determine the average flow field of the system. The cell size for these experiments was chosen to be 64×64 pixels. Bubble size characterisation was undertaken using a Photron FASTCAM SA3. This camera had a CMOS sensor which provided mega pixel resolution (1K by 1K pixels) up to 2,000 frames per second (fps). The captured images were processed using ImageJ, a public domain software for images editing, for determining the bubble size. Evaluations of bubble diameters and regime velocity were obtained from visual examination of the outcome of the High Speed Camera experiment. If N is the

number of bubbles crossing a given ideal horizontal plane in a time t and Q is the volume flow rate, then the average bubble volume can be evaluated by:

$$V_p = \frac{Qt}{N}, \quad (5)$$

and the diameter as:

$$d = \left(\frac{6}{\pi} V_p \right)^{1/3}. \quad (6)$$

Three CMC solutions were used (Section 2.3, Table 2) and for each of them, three different air flow rates were assessed. The values of Q , together with the measured quantities t and N and the resulting d are displayed in Table 3.

[Table 4 about here.]

The PIV technique detects the components of the Eulerian velocity field lying onto a given planar section of the fluid domain. A vertical plane, 3 cm away from the cylinder axis and parallel to the x axis was chosen for the scope:

$$\begin{cases} x \in (-X_{\max}, X_{\max}) \\ y \in (0, H) \\ z = Z_{\text{PIV}} \end{cases} \quad (7)$$

Here Z_{PIV} is the (constant) z coordinate at the PIV plane, $X_{\max} = (R^2 - Z_{\text{PIV}}^2)^{1/2}$, where R is the tank radius, and H is the tank height. This plane is referred to as the PIV plane hereafter.

Experiments were performed for each of the CMC solutions shown in Table 2, and each of the air flow rates shown in Table 3. Once the regime conditions for the flow and the bubbly motion had been reached (at least 2 minutes after the air flow rate had been set), the average field was measured over a time period of approximately 3 s

(being approximately the time between one bubble to reach the surface and the next one to do the same). The maximum experiment timescale was observed to be 0.34 s, which is one order of magnitude smaller than the PIV averaging time.

2.6. Average shear rate

The shear rate affects the bacteria populations involved into wastewater process (Gray, 2010)), and therefore average shear rate is a parameter of interest in environmental engineering design (Tchobanoglous et al., 2010). This approach is still in use, even if it has been pointed out (Camp and Stein, 1943; Clark, 1985) that a single number cannot represent a complex turbulent flow, in which areas of high input power coexist with dead zones (Sindall et al., 2013). Bridgeman (2012) performed CFD simulations on an impelled-stirred labscale digester and divided the domain into high, medium and low-velocity zones depending on the pointwise value of the velocity magnitude, and showed that a change in the impeller angular velocity does not affect the low-velocity zone relevantly.

Similarly, the shear rate value is expected to encompass several orders of magnitude due to coexistence of turbulent (around the bubbles) and relatively quiescent zones (Figure 5). Therefore it is appropriate to divide the domain into zones and compute the average shear rate therein. The purpose of the present work is to provide numerical validation for a CFD model, and therefore an analysis as in Bridgeman (2012) is out of scope. Nevertheless, it is fruitful to divide the domain into fixed, concentric zones, thus taking advantage of the axial symmetry, and compute the average shear rate therein. In this way, a single number can be associated to a relatively homogeneous zone, and then confronted with an analogous number calculated from the PIV data. This approach is simple as it uses only single numbers, but it is more meaningful than assessing simulated and experimental shear rate values averaged over the whole domain. This because, if the datum of the shear rate

259 averaged is over the whole domain, an element of granularity would be lost.

260 Assuming axis symmetry, Equation 4 reduces to:

$$261 \quad |\dot{\gamma}(r, y)| = \left| \frac{\partial u_r}{\partial y} + \frac{\partial u_y}{\partial r} \right|, \quad (8)$$

262 where r is the radial coordinate, and the tangential components of the shear stress are
263 suppressed due to the radial symmetry. Equation 8 can be rewritten in terms of x and
264 y , and thus evaluated on the PIV plane:

$$265 \quad |\dot{\gamma}(x, y)| = \sqrt{1 + \frac{Z_{\text{PIV}}^2}{x^2}} \left| \frac{\partial u_x}{\partial y} + \frac{\partial u_y}{\partial x} \right|. \quad (9)$$

266 The equation above can be discretized with a central differencing scheme. The
267 intervals $(-X_{\text{max}}, X_{\text{max}})$ and $(0, H)$ can be decomposed into $2N_x$ and N_y parts:

$$268 \quad \begin{aligned} -X_{\text{max}} \equiv x_{-N_x}, x_{-N_x+1}, \dots, x_{\alpha}, \dots, x_{N_x-1}, x_{N_x} \equiv X_{\text{max}} \\ 0, \dots, y_{\beta}, \dots, y_{N_y} \equiv H \end{aligned} \quad (10)$$

269 Then we have:

$$270 \quad |\dot{\gamma}|_{\alpha\beta} \approx \sqrt{1 + \frac{Z_{\text{PIV}}^2}{x_{\alpha}^2}} \left| \frac{u_{x,\alpha,\beta+1} - u_{x,\alpha,\beta-1}}{y_{\beta+1} - y_{\beta-1}} + \frac{u_{y,\alpha+1,\beta} - u_{y,\alpha-1,\beta}}{x_{\alpha+1} - x_{\alpha-1}} \right|. \quad (11)$$

271 The shear rate can be integrated over a volume domain comprised between two radii
272 r_a and r_b and height equal to the cylinder wet height, and divided by the volume of
273 the domain. This gives the average shear rate over that domain. r_a and r_b can be
274 rewritten as $(x_a^2 + z^2)^{1/2}$ and $(x_b^2 + z^2)^{1/2}$ respectively, where x_a and x_b are the x
275 components of r_a and r_b respectively. A change of integration variables from r to x
276 thus allows us to express the average shear rate in terms of x and y , and to evaluate it

277 by integrating over the PIV plane. x_a and x_b can be rewritten as aX_{\max} and bX_{\max} :

$$278 \quad \langle \dot{\gamma} \rangle_a^b = \frac{2}{X_{\max}^2 H (b^2 - a^2)} \int_0^H dy \quad (12)$$

$$\frac{1}{2} \left(\int_{-bX_{\max}}^{-aX_{\max}} + \int_{aX_{\max}}^{bX_{\max}} \right) dx \sqrt{x^2 + Z_{\text{PIV}}^2} |\dot{\gamma}(x, y)| .$$

279 The expression above can be evaluated numerically with the rectangle rule method:

$$280 \quad \langle \dot{\gamma} \rangle_a^b \approx \frac{2}{X_{\max}^2 H (b^2 - a^2)} \sum_{\beta=0}^{N_y} \frac{1}{2} \left(\sum_{\alpha=-b}^{-a} + \sum_{\alpha=a}^b \right) \quad (13)$$

$$\frac{x_{\alpha+1} - x_{\alpha-1}}{2} \frac{y_{\beta+1} - y_{\beta-1}}{2} \sqrt{x_{\alpha}^2 + Z_{\text{PIV}}^2} |\dot{\gamma}|_{\alpha\beta} ,$$

281 3. CFD

282 3.1. Model strategy

283 According to Andersson et al. (2012), an Euler-Lagrange (EL) model is preferable for
 284 multiphase modelling, provided that the number of particles is not so high as to
 285 render the computational cost prohibitive, and Sungkorn et al. (2011) employed the
 286 Euler-Lagrange model to simulate a bubble column rising in a Newtonian liquid.
 287 Sungkorn et al. (2012) subsequently employed the same model to simulate the motion
 288 of gas bubbles inside a non-Newtonian fluid mixed by a stirrer. The work reported in
 289 this paper followed this approach, and an Euler-Lagrange model in which the liquid
 290 and bubble phase are coupled together was employed.

291 In a full-scale plant, the bubbles rise in vertical columns the diameter of which is small
 292 compared with the digester size. Therefore, the focus of the work reported here was
 293 on resolving the flow patterns away from the bubble plume rather than describing the
 294 bubble motion in detail. For this reason, the following approximations were adopted:
 295 (i) bubble-bubble interactions were neglected; (ii) effects on fluid motion due to
 296 deformations of the bubble surface were neglected—this is equivalent to considering

the bubbles to be spherical; (iii) bubbles were considered to be pointwise. These approximations do not allow a detailed description of the flow in close proximity to the bubbles, but do reproduce an interphase momentum transfer sufficiently accurate to reproduce the flow patterns away from the bubble column satisfactorily.

3.2. Liquid phase

In the EL model, the Navier-Stokes equations for the continuous phase are solved in conjunction with the equations of motion of the individual particles (Andersson et al., 2012). This coupling is realized by adding a momentum-transfer term to the equation. Thus the Navier-Stokes equations become:

$$\nabla \cdot \mathbf{u} = 0 ; \quad (14)$$

$$\rho \partial_t \mathbf{u} + \rho \nabla \cdot (\mathbf{u} \otimes \mathbf{u}) = -\nabla p + \nabla \cdot \tau + \rho \mathbf{g} + \mathbf{F} , \quad (15)$$

The viscosity τ has been defined in Equation 1. The term \mathbf{F} is due to momentum exchange between fluid and particles. Further details on this term are explained in Section 3.3.

3.3. Bubble phase

The term \mathbf{F} in Eq. 15 represents the momentum transfer between the fluid phase and each individual bubble (van Wachem and Almstedt, 2003) and can be expressed as follows:

$$\mathbf{F}(\mathbf{x}) = \sum_p \mathbf{F}_p \delta(\mathbf{x} - \mathbf{x}_p) , \quad (16)$$

where \mathbf{F}_p is the resultant of the forces acting on the p -th bubble. The Dirac delta, after discretization, states that the contribution of the p -th bubble to Eq. 15 is \mathbf{F}_p in

the cell in which the bubble is present, and zero elsewhere. The equation of motion for each bubble is Newton's second law:

$$m_p \dot{\mathbf{u}}_p = \mathbf{F}_p , \quad (17)$$

where $\mathbf{u}_p \equiv \dot{\mathbf{x}}_p$ is the instantaneous velocity of the bubble. The resultant for the p -th bubble can be expressed as in Deen et al. (2004)

$$\mathbf{F}_p = \mathbf{F}_p^a + \mathbf{F}_p^b + \mathbf{F}_p^d + \mathbf{F}_p^\ell , \quad (18)$$

that is: added mass, pressure gradient, buoyancy, drag, lift. We have:

$$\mathbf{F}_p^a = C_a \rho V_p (D_t \mathbf{u} - d_t \mathbf{u}_p) , \quad (19)$$

$$\mathbf{F}_p^b = V_p (\rho_p - \rho) \mathbf{g} , \quad (20)$$

$$\mathbf{F}_p^d = \frac{1}{2} C_d \rho \pi \frac{d_p^2}{4} |\mathbf{u} - \mathbf{u}_p| (\mathbf{u} - \mathbf{u}_p) , \quad (21)$$

$$\mathbf{F}_p^\ell = C_\ell \rho V_p (\mathbf{u} - \mathbf{u}_p) \wedge \nabla \wedge \mathbf{u} . \quad (22)$$

Here D_t indicates the total temporal derivative and reads $D_t \equiv \partial_t + \mathbf{u} \cdot \nabla$. The coefficients C_a and C_ℓ can be expressed as in the model proposed by Dewsbury et al. (1999), that is specific for gas bubbles and light solid particles rising in pseudoplastic liquids, and Tomiyama et al. (2002):

$$C_a = \frac{1}{2} , \quad (23)$$

338

339

$$C_\ell = \begin{cases} \min [0.288 \tanh (0.121 \text{Re}_p) , & \text{Re}_p \leq 4 , \\ f(\text{Eo}_d)] , & \\ f(\text{Eo}_d) , & 4 < \text{Re}_p \leq 10 , \\ - 0.29 , & \text{Re}_p > 10 , \end{cases} \quad (24)$$

340 where:

341

$$f(\text{Eo}_d) = 0.00105 \text{Eo}_d^3 - 0.0159 \text{Eo}_d^2 - 0.0204 \text{Eo}_d + 0.474 . \quad (25)$$

342 Eo_d is the modified Eötvös number and is defined as $(\rho_p - \rho) d_{d,p}^2 / \sigma$, where $d_{d,p}$ is the
343 maximum horizontal dimension of the p -th bubble. Since here the bubbles are
344 considered to be spherical, $d_{d,p}$ is the bubble diameter. C_d is a function of the bubble
345 Reynolds number (Dewsbury et al., 1999):

346

$$C_d = \begin{cases} \frac{16}{\text{Re}_p} (1 + 0.173 \text{Re}_p^{0.657}) & \text{Re}_p \leq 195 , \\ + \frac{0.413}{1 + 16,300 \text{Re}_p^{-1.09}} , & \\ 0.95 , & \text{Re}_p > 195 . \end{cases} \quad (26)$$

347 The bubble Reynolds number Re_p is defined as:

348

$$\text{Re}_p = \frac{\rho d U_t}{\mu} , \quad (27)$$

349 where U_t is the velocity scale and is evaluated as the modulus of the difference
350 between the bubble velocity and the fluid velocity in the bubble surroundings. During

the simulation runs, the value of Re_p is evaluated from Equation 27 and the value of μ calculated is described in Section 2.2, for every point \mathbf{r} and time t . The field $Re_p(\mathbf{r}, t)$ thus obtained is used as an input to compute the velocity field.

3.4. Mesh

Each simulation was run in parallel on three dual-processor 8-core 64-bit 2.2 GHz Intel Sandy Bridge E5-2660 worker nodes with 32 GB of memory, for a total of 48 nodes. Six grids were generated for this study all with different cell numbers, but with the same structure. Details of the grids are summarised in Table 4, and an example is shown in Figure 3.

[Table 5 about here.]

[Figure 3 about here.]

The presence of a central column of bigger cells (Figure 3) is noteworthy. The bubble diameter is approximately 7 to 13 mm (cfr. Table 3). Thus, any mesh that can successfully reproduce the dynamics of this system should be formed by cells much smaller than a single bubble. However, this contradicts the assumption made earlier, that the bubbles are pointwise, and, more generally, a requirement for an Euler-Lagrange simulation that states that the parcel size should be much smaller than the cell size (van Wachem and Almstedt, 2003; Andersson et al., 2012). However, recent research (Sungkorn et al., 2011, 2012) demonstrated that this requirement can be relaxed if the number of bubbles remains “small”. In the research cited above, the number of bubbles present in the system was of the order of $O(10^4)$ and therefore, the term “small” can be intended as “smaller than 10^4 ”. It should be noted that that in Sungkorn et al. (2011, 2012) the continuous liquid phase was modelled using the lattice-Boltzmann method; that is not the case in the work

375 reported here. However, the considerations above refer to the discrete bubble phase,
 376 the modelling of which is independent from the continuous phase. Therefore, it is
 377 appropriate to adopt the considerations of Sungkorn et al. (2011, 2012) for the bubble
 378 phase as valid also for the present work.

379 Nevertheless, it was observed in this study that the flow patterns depend strongly on
 380 the grid size when cells are much smaller than the bubbles. For this reason, larger
 381 cells, of the order of magnitude of the bubbles' volumes or slightly larger, were placed
 382 along the bubbles' expected trajectory.

383 Regarding the simulation of bubble injection, during the simulation, a bubble is
 384 "created" at certain times, in a place near the bottom of the tank, such that its centre
 385 lies along the cylinder axis, at about 5 to 11 mm from the bottom, and its velocity is
 386 zero. The reality is somewhat different, as a bubble takes non-zero time to expand out
 387 of the nozzle and then detaches with a non-zero velocity. The expansion of a bubble
 388 pushes upwards the water column above it; this may give rise to a liquid recall from
 389 the external zones near the bottom towards the centre in the lower part of the tank,
 390 and to an increase of the velocity of the liquid phase around the column above it.

391 Both these possible effects are neglected in the model.

392 The liquid motion arises from momentum transfer from bubbles to liquid. As the
 393 bubbles are expected to form a vertical plume, it is reasonable to suppose that the
 394 turbulent Reynolds stress tensor R is not isotropic. Of the Reynolds stress models,
 395 the Launder-Reece-Rodi model takes into account both slow and rapid pressure strain
 396 terms of the Reynolds tensor, and it is the first that has been widely used (Pope,
 397 2000). The Launder-Gibson model (Gibson and Launder, 1978), in addition to the
 398 former, takes into account the redistribution of normal stresses near the walls
 399 (ANSYS, 2012). It was considered that the wall effects may be of interest in the
 400 present study, and therefore the latter model was chosen.

401 The timestep was defined indirectly and dynamically by an algorithm aimed at
 402 keeping the maximum Courant number just below a specified limit of 0.2. The
 403 Courant number is a quantity defined for every cell such that given a cell labelled i ,
 404 let be $|\mathbf{u}_i|$ the velocity magnitude, L_i the length dimension along \mathbf{u}_i and Δt the
 405 timestep, then the Courant number for the cell i is:

$$406 \quad Co_i = \frac{|\mathbf{u}_i| \Delta t}{L_i} . \quad (28)$$

407 The maximum Courant number, Co , is the maximum value of Co_i over i . Starting
 408 from a small initial timestep (in this work, 10^{-5} s) the timestep was assessed in order
 409 to keep the maximum Courant number as near as possible to, but smaller than, the
 410 limit value of 0.2.

411 The initial conditions are reported in Table 5.

412 [Table 6 about here.]

413 Initially, a series of (transient) first-order runs was performed to simulate the
 414 development of the bubble column from a state in which no liquid phase motion and
 415 no bubbles were present in the system. As the object of study in this work is the
 416 liquid phase motion in presence of a fully-developed bubble column, the sole use of
 417 these first series of runs was to provide the initial conditions for the main (transient)
 418 second-order runs. The latter provided the data relative to the behaviour of the
 419 system in the presence of the fully-developed bubble column, and were compared with
 420 the experimental data.

421 The boundary conditions for the preliminary runs are shown in Table 5. The initial
 422 conditions for the preliminary runs were: $4.95 \cdot 10^{-4} \text{ m}^2 \text{ s}^{-3}$ for the ε field; zero for the
 423 other fields (p , u , R). The differencing schemes were: linear for interpolations, limited
 424 central differencing for the Gradient operator, linear for the Laplacian, Van Leer for

all the other spatial operators. For the preliminary runs, the first-order Eulerian scheme for the time derivative was used; however, for the main runs, the second-order backward scheme was used.

CFD runs were performed for each of the CMC solutions as in Table 2, and each of the air flow rates of Table 3. The CFD output consists of a series of binary files arranged into directories, one for each timestep recorded. Binary files were collected for times corresponding to integer seconds after the initial conditions. The preliminary runs were performed for a simulation time of 10 s; then, their final timesteps were used as initial conditions for the main simulations, which were run for an additional simulation time of 50 s, for a total time of 60 s.

The binary files were processed to extract data to be compared with the PIV data. The Eulerian velocity field was interpolated onto the PIV plane. Then, the components parallel to the plane were averaged over time. As only the flow pattern originating from a fully-developed bubble column is of interest in this work, the preliminary times were not included into the average. Also the first ten seconds of the main runs were disregarded in order to avoid the artificial transience from first-order to second-order solutions. Thus, only the last (second-ordered) 40 seconds of each run were included in the average.

Despite the increase of the number of equations to be solved due to the choice of a Reynolds-stress turbulence model, the computational expense remained acceptable as the runtime remained below 30 hours per run. The timestep was observed to be between 0.0004 to 0.02 s. The number of bubbles present in the system at a given time was always less than 20 in all the runs. This kind of model is the ideal approach for dispersed phase systems (Andersson et al., 2012), and undoubtedly this model has benefitted from the small number of bubbles in terms of reduced computational expense compared with other options.

451 3.5. Impact of Central Cells Size

452 [Figure 4 about here.]

453 A preliminary series of runs was performed in order to verify that the flow patterns
 454 were stable under variations of the central cells size. The configuration labelled as
 455 cmc04-2 in Table 3 was tested with the Grids 4a, 4 and 4b described in Table 4 and
 456 the outcome is shown in Figure 4. The graphs show the magnitude of the velocity
 457 along three vertical lines lying on the PIV plane, respectively at 0.4, 0.6 and 0.8
 458 half-widths from the central axis projection. There is a general good agreement
 459 between the three grids: small differences are either inside experimental errors
 460 ($r/R=0.8$ and $r/R=0.6$), or are confined to limited domain zones, such as near the
 461 surface, around the central axis ($r/R=0.4$ and, less, $r/R=0.6$).

462 3.6. Dependence from the mesh size

463 The Grid Convergence Index (GCI) proposed by Roache (1998) has become a
 464 standard method for assessing the independence of the CFD results from the mesh
 465 size and determining a measure of the error. According with Celik et al. (2008), a
 466 variable ϕ critical to the conclusions of the work is determined from three sets of
 467 grids, say a , b and c from the finest to the coarsest. The underlying hypothesis is that
 468 the value of ϕ determined by the simulation can be written as a Taylor polynomial
 469 (not necessarily infinite; therefore the Taylor polynomial may not be a Taylor series)
 470 of the grid spacing h :

$$471 \quad \phi = \phi_{\text{exact}} + g_1 h + g_2 h^2 + g_3 h^3 + \dots \quad (29)$$

472 The apparent order of convergence p is calculated recursively in the following way:

$$\begin{aligned}
 p &= \frac{1}{\ln r_{ba}} |\ln |\varepsilon_{cb}/\varepsilon_{ba}| + p(q)| \\
 473 \quad q(p) &= \ln \frac{r_{ba}^p - s}{r_{cb}^p - s} \\
 s &= \text{sign}(\varepsilon_{cb}/\varepsilon_{ba})
 \end{aligned} \tag{30}$$

474 where r_{cb} and r_{ba} are the linear refinement factors from mesh c to b and from mesh b
 475 to mesh a respectively, and:

$$476 \quad \varepsilon_{cb} \equiv \phi_c - \phi_b, \quad \varepsilon_{ba} \equiv \phi_b - \phi_a. \tag{31}$$

477 The grid convergence index (GCI) is defined as:

$$478 \quad \text{GCI}_{cb} \equiv \frac{1.25 |\varepsilon_{cb}/\phi_b|}{r_{cb} - 1}, \quad \text{GCI}_{ba} \equiv \frac{1.25 |\varepsilon_{ba}/\phi_b|}{r_{ba} - 1}. \tag{32}$$

479 The simulations are in the asymptotic range of convergence (and hence mesh
 480 independence is achieved) when

$$481 \quad \frac{\text{GCI}_{cb}}{r_{ba}^p \text{GCI}_{ba}} \simeq 1. \tag{33}$$

482 Under these circumstances, the value of GCI_{ba} can be used as a (conservative)
 483 estimation of the relative error on the finest mesh.

484 **4. Results and discussion**

485 The main runs comprised nine series, one for each of the configurations described in
 486 Table 2. In each series, the Grids 1, 2, 3 and 4 described in Table 4 were tested.

4.1. Assessment of the mesh dependence

A GCI analysis was carried out as described in Section 3.6. As the critical variable, the average shear rate over the whole computational domain was chosen. Two tests were performed for each run series, one involving grids 1,2 and 3, and another one involving grids 2, 3 and 4. The results are shown in Tables 6, 7 and 8.

[Table 7 about here.]

[Table 8 about here.]

[Table 9 about here.]

In most of the runs, the asymptotic convergence is reached for grid 2, but lost in grid 1. Oscillations are reported in the run series cmc02-2 and cmc04-2, with grid 1 behaving slightly better than grid 2 for the former series, and the converse for the latter. For the runs cmc04-1 and cmc04-3 the situation is less clear. This behaviour is to be expected because, as explained in Section 3.4, there is a lower limit for the mesh size, dependant on the bubble size. Therefore, the GCI underlying hypothesis Equation 29 does not hold. Consequently, it is expected that the critical variable converges to, or oscillates around, a limit value for decreasing values of h , but still larger than the lower limit. Below this limit, the simulation is expected to produce unphysical results, and therefore the asymptotic convergence is lost. The GCI test gives an indication whether the mesh is fine enough to achieve the asymptotic convergence range. However, in this context, it can give additional information about whether the mesh is too fine if compared with the bubble size. It can be concluded that the grid 1 is too fine, and that the grid 2 is optimal for all the runs except for the series cmc02-2, where the grid 1 is superior.

510 4.2. Analysis of the Velocity Field

511 Figure 5 shows a series of comparisons between PIV outcome and simulation, for the
 512 example cases labelled as cmc02-2, cmc04-2 and cmc08-2. Grid 1 was used in all the
 513 cases. The simulations reproduce well the measured flow both in magnitude and in
 514 flow shape. Also the position of the centre of the vortices correlates well with the PIV
 515 outcome. The principal differences between simulation and PIV consist of: (i)
 516 under-estimated velocity magnitude around the bubble column, especially at the
 517 bottom; (ii) slightly over-estimated velocity in the upper part of the tank; and (iii)
 518 slightly under-estimated velocity in the lower part of the tank.

519 [Figure 5 about here.]

520 Examination of Figure 5 indicates that (i) is the most significant difference. In this
 521 regard, it should be noted that the bubble column was interposed between the PIV
 522 plane and the camera. Therefore, there is a refraction effect of the laser rays through
 523 the bubbles and thus the PIV data may be less robust in the inner parts of the
 524 domain. As an example of this, by a simple application of the Snell's law with
 525 standard values for the refraction coefficients of air (1.000) and water (1.333), it can
 526 be noted that a laser beam scattering into a bubble with an impact parameter of half
 527 the bubble radius is deflected of an angle of 20.5° . Nevertheless, explanations
 528 concerning the nature and the approximations of the theoretical model can be
 529 elaborated. In particular:

530 (i) for under-estimation of velocity magnitude there are three possible causes. First,
 531 the cells along the central column are much larger than any other cell, and there are
 532 only 10 to 12 along the whole tank height (see Table 4). Thus, there may be too few
 533 cells to expect an accurate description of the flow near the central axis. The second
 534 source of error may be related to the way the parcels are introduced into the system.

535 The implications of this simplification, in particular regarding the possible increase of
 536 liquid phase velocity in the central column, have been discussed in Section 3.4. A final
 537 cause for this difference may be the fact that, due to the assumption made in Section
 538 3.1, the model may simply be unable to reproduce the flow in the immediate
 539 surroundings of a bubble.

540 For (ii) the cause of over-estimation of velocity in the upper part of the tanks may lie
 541 in the description of the liquid-atmosphere interface. It was observed that the bubble
 542 column gives rise to a water hump just above it, and to vertical oscillations along the
 543 whole interface. This phenomenon is more evident when the viscosity decreases
 544 (Figure 6). The fraction of the bubbles' kinetic energy that is transferred to the liquid
 545 phase is then redistributed as kinetic energy and potential energy of the mass
 546 displaced into the hump, and also to the air above due to the interface oscillations. In
 547 the simulations, however, the interface is modelled as a rigid non-slip surface, and no
 548 liquid displacement is possible, nor is any energy transfer to the air. The transferred
 549 energy is therefore not redistributed, and remains in the form of liquid kinetic energy.
 550 Thus, the simulations over-estimate the velocity field magnitude especially in the
 551 regions where the energy redistribution should (but does not) take place, i.e. near the
 552 interface or just below it.

553 [Figure 6 about here.]

554 In the case of (iii) as before, velocity under-estimation in the lower part of the tank
 555 may once again be due to the way the bubbles are introduced into the system. The
 556 implications of this simplification, in particular with regard to the possible liquid
 557 recall from the external zones, have been discussed in Section 3.4.

558 All runs' outcomes are displayed in Figure 7 (2 g l^{-1} solution), Figure 8 (4 g l^{-1}
 559 solution) and Figure 9 (8 g l^{-1} solution). The graphs show the magnitude of the

560 projected velocity along three vertical lines lying on the PIV plane, respectively at
 561 0.4, 0.6 and 0.8 half-widths from the central axis projection, as shown in Figure 4.
 562 The runs were carried out with Grids 1,2,3 and 4. There is a good general agreement
 563 between the different grids. In particular, the differences are smaller when the CMC
 564 concentration increases. The runs with larger mesh size (especially Grid 4)
 565 sporadically differ in the lower concentrations, in particular in the 2 g l^{-1} .
 566 In general, the experimental data are well reproduced by the computational runs.
 567 Only the local minima on the $r/R=0.4$ runs are not very well reproduced. This
 568 corresponds to a slight misplacement of the main vortices towards the central axis, as
 569 can also be noted in Figure 5. The effect is more marked when the CMC
 570 concentration increases. Nevertheless, the agreement, even quantitatively, is good.

571 [Figure 7 about here.]

572 [Figure 8 about here.]

573 [Figure 9 about here.]

574 *4.3. Average Shear Rate calculation*

575 Figure 10 depicts the average shear rate over different domains. It is evident that the
 576 major discrepancies between experimental and simulated data are concentrated in the
 577 inner part of the domain—between 0 and $0.2X_{\max}$, and, to a lesser extent, between
 578 $0.2X_{\max}$ and $0.5X_{\max}$. As expected, there is no agreement between computational and
 579 PIV data between 0 and $0.2X_{\max}$, for the reasons discussed above. However, the
 580 agreement is good in the external part of the domain, between $0.5X_{\max}$ and X_{\max} .
 581 This result can be considered satisfactory because it provides a further confirmation
 582 that the CFD model presented in this work is able to reproduce the flow patterns in
 583 the zone of interest for the anaerobic digestion design, that is, away from the bubble
 584 column.

585 Interestingly, the average shear rate values are comprised between 0.1 and 1 s^{-1} , well
 586 below the value of $50\text{-}80 \text{ s}^{-1}$ suggested by literature for anaerobic digestion plants
 587 (Tchobanoglous et al., 2010). Similarly, low values of shear rate magnitude compared
 588 with the literature were found also in Bridgeman (2012), where it was observed that
 589 the presence of dead or low-mixed zones could not be avoided even by increasing the
 590 power input, and that this fact did not affect the biogas production.

591 [Figure 10 about here.]

592 5. Conclusions

593 A novel EL model for gas-mixing in anaerobic digestion was developed.
 594 The model was validated with lab-scale data, under the most adverse
 595 circumstances—that is, bubble sizes not negligible when compared with cells sizes.
 596 The relative simplicity of the viscosity model did not affect the results of the
 597 simulations. It would be interesting to test more complex viscosity models in future
 598 works. The design of the solver facilitates the addition of other types of Lagrangian
 599 particles; and this aspect may be used to introduce sedimenting particles.
 600 Care must be adopted in choosing the appropriate mesh resolution. In particular, a
 601 mesh that is too fine may be detrimental for mesh independence; for this reason, a
 602 mesh independence test such as GCI is essential.
 603 Because of the refraction of the laser rays through the gas bubbles, the PIV technique
 604 can give unreliable results in the regions near the bubble column. The fact that the
 605 flow away from the bubble column is satisfactorily reproduced suggests that the
 606 bubble-liquid phase momentum transfer is modelled with a sufficient degree of
 607 accuracy, but further research with different experimental techniques is desirable to
 608 measure the flow in the regions near the bubble column.

In conclusion, in the zones of interest for purposes of full-scale simulations, the model reproduces the experimental data robustly and with fidelity. Therefore, it can be successfully employed for full-scale predictions.

Acknowledgements

The computational work reported in this paper was undertaken using the BlueBEAR high performance computing facility at the University of Birmingham, UK. The authors are grateful for the facility and support provided by the University.

The laboratory work was undertaken under the supervision of Prof Mark Simmons; his contribution is gratefully acknowledged.

The first author is funded via a University of Birmingham Postgraduate Teaching Assistantship award.

References

- Achkari-Begdouri, A., Goodrich, P.R., 1992. Rheological properties of dairy cattle manure. *Bioresour. Technol.* 40, 149–156. doi:10.1016/j.biortech.2004.06.020.
- Andersson, B., Andersson, R., Håkansson, L., Mortensen, M., Defence, N., Sudiyo, R., van Wachem, B., 2012. *Computational Fluid Dynamics for Engineers*. Cambridge University Press.
- ANSYS, 2012. *ANSYS FLUENT 14.5 Theory Guide*. ANSYS, Inc.
- Baudez, J.C., Slatter, P., Eshtiaghi, N., 2013. The rheological behaviour of anaerobic digested sludge. *Chem. Eng. J.* 215–216, 182–187. URL: <http://dx.doi.org/10.1016/j.watres.2011.08.035>, doi:10.1016/j.cej.2012.10.099.

- 631 Bridgeman, J., 2012. Computational fluid dynamics modelling of sewage sludge
 632 mixing in an anaerobic digester. *Adv. Eng. Softw.* 44, 54–62. URL:
 633 <http://dx.doi.org/10.1016/j.advengsoft.2011.05.037>,
 634 doi:10.1016/j.advengsoft.2011.05.037.
- 635 Camp, T.R., Stein, P.C., 1943. Velocity gradients and internal work in fluid motion.
 636 *J. Bost. Soc. Civ. Eng.* 85, 218–237.
- 637 Celik, I.B., Ghia, U., Roache, P.J., Freitas, C.J., Coleman, H., Raad, P.E., 2008.
 638 Procedure for Estimation and Reporting of Uncertainty Due to Discretization in
 639 CFD Applications. *J. Fluids Eng.* 130, 078001. doi:10.1115/1.2960953.
- 640 Clark, M.M., 1985. Critique of Camp and Stein's RMS velocity gradient. *J. Environ.*
 641 *Eng.* I, 741–754.
- 642 Deen, N.G., van Sint Annaland, M., Kuipers, J.A.M., 2004. Multi-scale modeling of
 643 dispersed gas-liquid two-phase flow. *Chem. Eng. Sci.* 59, 1853–1861.
 644 doi:10.1016/j.ces.2004.01.038.
- 645 Dewsbury, K., Karamanev, D., Margaritis, a., 1999. Hydrodynamic characteristics of
 646 free rise of light solid particles and gas bubbles in non-Newtonian liquids. *Chem.*
 647 *Eng. Sci.* 54, 4825–4830. doi:10.1016/S0009-2509(99)00200-6.
- 648 Gibson, M.M., Launder, B.E., 1978. Ground effects on pressure fluctuations in the
 649 atmospheric boundary layer. *J. Fluid Mech.* 86, 491–511.
 650 doi:10.1017/S0022112078001251.
- 651 Gómez, X., Cuertos, M.J., Cara, J., Morán, a., García, a.I., 2006. Anaerobic
 652 co-digestion of primary sludge and the fruit and vegetable fraction of the municipal
 653 solid wastes. Conditions for mixing and evaluation of the organic loading rate.
 654 *Renew. Energy* 31, 2017–2024. doi:10.1016/j.renene.2005.09.029.

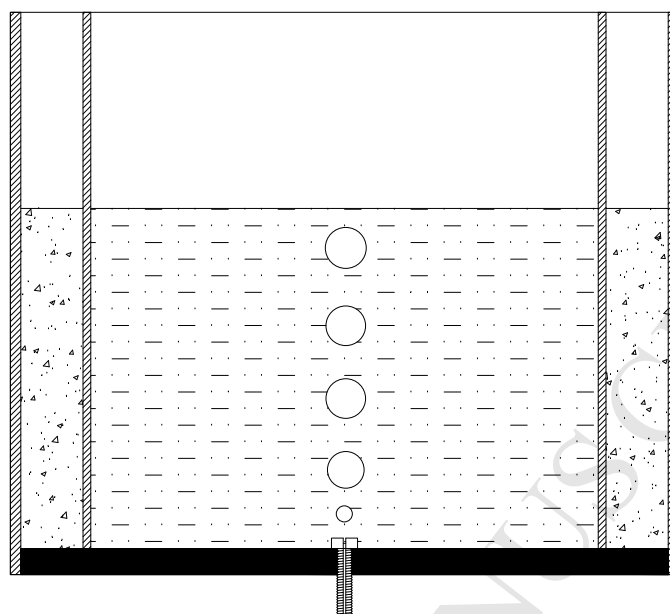
- Gray, N.F., 2010. Water Technology: An Introduction for Environmental Scientists and Engineers. IWA Publishing. doi:10.1016/B978-1-85617-705-4.00026-5.
- Karim, K., Thoma, G.J., Al-Dahhan, M.H., 2007. Gas-lift digester configuration effects on mixing effectiveness. Water Res. 41, 3051–3060. doi:10.1016/j.watres.2007.03.042.
- McMahon, K.D., Stroot, P.G., Mackie, R.I., Raskin, L., 2001. Anaerobic codigestion of municipal solid waste and biosolids under various mixing conditions-II: Microbial population dynamics. Water Res. 35, 1817–1827. doi:10.1016/S0043-1354(00)00438-3.
- Ong, H.K., Greenfield, P.F., Pullammanappallil, P.C., 2002. Effect of mixing on biomethanation of cattle-manure slurry. Environ. Technol. 23, 1081–1090.
- Pope, S.B., 2000. Turbulent Flows. Cambridge University Press.
- Roache, P.J., 1998. Verification of codes and calculations. AIAA J. 36, 696–702. doi:10.2514/3.13882.
- Sindall, R.C., Bridgeman, J., Carliell-Marquet, C., 2013. Velocity gradient as a tool to characterise the link between mixing and biogas production in anaerobic waste digesters. Water Sci. Technol. 67, 2800–2806. doi:10.2166/wst.2013.206.
- Stroot, P.G., McMahon, K.D., Mackie, R.I., Raskin, L., 2001. Anaerobic codigestion of municipal solid waste and biosolids under various mixing conditions-I. digester performance. Water Res. 35, 1804–1816. doi:10.1016/S0043-1354(00)00439-5.
- Succi, S., 2001. The Lattice Boltzmann Equation for Fluid for Fluid Dynamics and Beyond. doi:10.1016/0370-1573(92)90090-M.

- 677 Sungkorn, R., Derksen, J.J., Khinast, J.G., 2011. Modeling of turbulent gas-liquid
678 bubbly flows using stochastic Lagrangian model and lattice-Boltzmann scheme.
679 Chem. Eng. Sci. 66, 2745–2757. URL:
680 <http://dx.doi.org/10.1016/j.ces.2011.03.032>,
681 doi:10.1016/j.ces.2011.03.032.
- 682 Sungkorn, R., Derksen, J.J., Khinast, J.G., 2012. Modeling of aerated stirred tanks
683 with shear-thinning power law liquids. Int. J. Heat Fluid Flow 36, 153–166. URL:
684 <http://dx.doi.org/10.1016/j.ijheatfluidflow.2012.04.006>,
685 doi:10.1016/j.ijheatfluidflow.2012.04.006.
- 686 Tchobanoglous, G., Burton, Franklin, L., Stensel, H.D., 2010. Wastewater
687 Engineering. Metcalf & Eddy, Inc.
- 688 Terashima, M., Goel, R., Komatsu, K., Yasui, H., Takahashi, H., Li, Y.Y., Noike, T.,
689 2009. CFD simulation of mixing in anaerobic digesters. Bioresour. Technol. 100,
690 2228–2233. URL: <http://dx.doi.org/10.1016/j.biortech.2008.07.069>,
691 doi:10.1016/j.biortech.2008.07.069.
- 692 Tomiyama, A., Tamai, H., Zun, I., Hosokawa, S., 2002. Transverse migration of single
693 bubbles in simple shear flows. Chem. Eng. Sci. 57, 1849–1858.
694 doi:10.1016/S0009-2509(02)00085-4.
- 695 Versteeg, H.K., Malalasekera, W., 1995. An introduction to Computational Fluid
696 Dynamics. Longman Scientific & Technical.
- 697 Vesvikar, M.S., Al-Dahhan, M.H., 2005. Flow pattern visualization in a mimic
698 anaerobic digester using CFD. Biotechnol. Bioeng. 89, 719–732.
699 doi:10.1002/bit.20388.

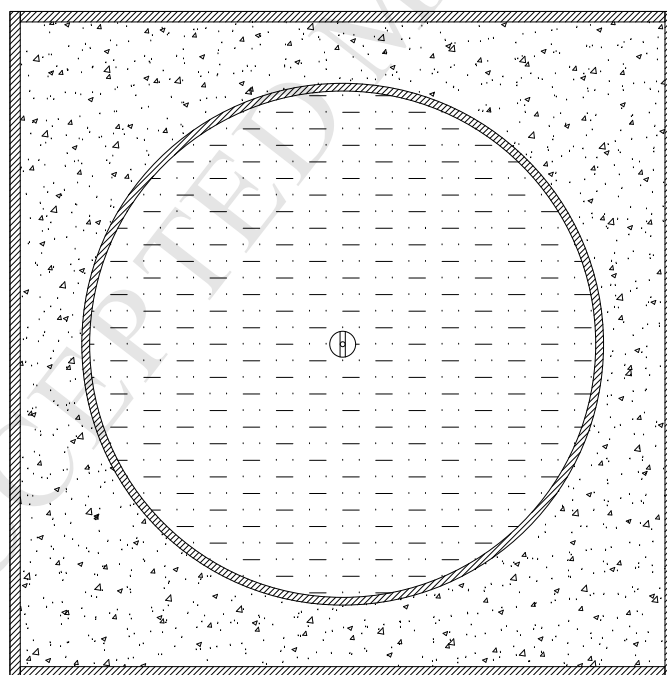
- 700 van Wachem, B.G.M., Almstedt, A.E., 2003. Methods for multiphase computational
701 fluid dynamics. *Chem. Eng. J.* 96, 81–98. doi:10.1016/j.cej.2003.08.025.
- 702 Ward, A.J., Hobbs, P.J., Holliman, P.J., Jones, D.L., 2008. Optimisation of the
703 anaerobic digestion of agricultural resources. *Bioresour. Technol.* 99, 7928–7940.
704 doi:10.1016/j.biortech.2008.02.044.
- 705 Wolf-Gladrow, D., 2005. *Lattice-Gas Cellular Automata and Lattice Boltzmann*
706 *Models*. Springer.
- 707 Wu, B., 2010. CFD simulation of gas and non-Newtonian fluid two-phase flow in
708 anaerobic digesters. *Water Res.* 44, 3861–3874. URL:
709 <http://dx.doi.org/10.1016/j.watres.2010.04.043>,
710 doi:10.1016/j.watres.2010.04.043.
- 711 Wu, B., 2012. Integration of mixing, heat transfer, and biochemical reaction kinetics
712 in anaerobic methane fermentation. *Biotechnol. Bioeng.* 109, 2864–2874.
713 doi:10.1002/bit.24551.
- 714 Wu, B., 2014. CFD simulation of gas mixing in anaerobic digesters. *Comput.*
715 *Electron. Agric.* 109, 278–286. URL:
716 <http://www.sciencedirect.com/science/article/pii/S0168169914002543>,
717 doi:10.1016/j.compag.2014.10.007.
- 718 Wu, B., Chen, S., 2008. CFD simulation of non-Newtonian fluid flow in anaerobic
719 digesters. *Biotechnol. Bioeng.* 99, 700–711. doi:10.1002/bit.21613.

720 **List of Figures**

721	1	Experimental rig top and front view. Pump, flowmeter, pipes and fittings	
722		not shown.	34
723	2	Shear rate-shear stress dependance. Points: measured values. Lines:	
724		best fits.	35
725	3	Example of the grids described in Table 4.	36
726	4	Preliminary series along a vertical axis against PIV outcome. Red: Grid	
727		4a. Blue: Grid 4. Green: Grid 4b.	37
728	5	Projected velocity plots using the Grid 1. cfd02-2: (a): PIV outcome,	
729		(b): CFD simulation. cfd04-2: (c): PIV outcome, (d): CFD simulation.	
730		cfd08-2: (e): PIV outcome, (f): CFD simulation.	38
731	6	Liquid-air interface. (a): cmc02-1. (b): cmc02-2. (c): cmc02-3. (d):	
732		cmc04-1. (e): cmc04-2. (f): cmc04-3. (g): cmc08-1. (h): cmc08-2. (i):	
733		cmc08-3.	39
734	7	CFD-simulated velocity magnitude along a vertical axis against PIV out-	
735		come. 2 g l^{-1}	40
736	8	CFD-simulated velocity magnitude along a vertical axis against PIV out-	
737		come. 4 g l^{-1}	41
738	9	CFD-simulated velocity magnitude along a vertical axis against PIV out-	
739		come. 8 g l^{-1}	42
740	10	Average shear rate over different subdomains: comparison between ex-	
741		perimental and simulated data. Below: ratio between simulated and	
742		experimental data.	43



(a)



(b)

Figure 1 *Experimental rig top and front view. Pump, flowmeter, pipes and fittings not shown.*

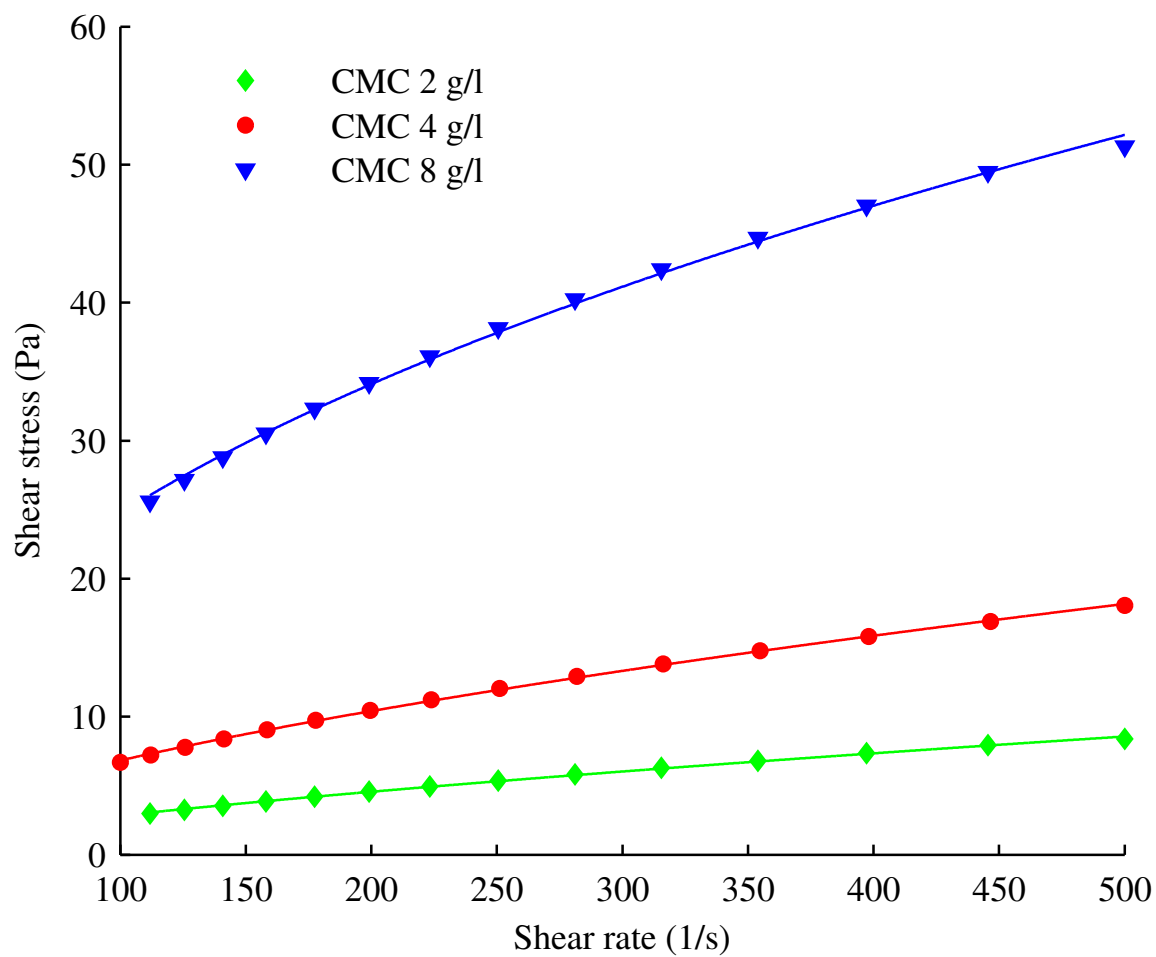
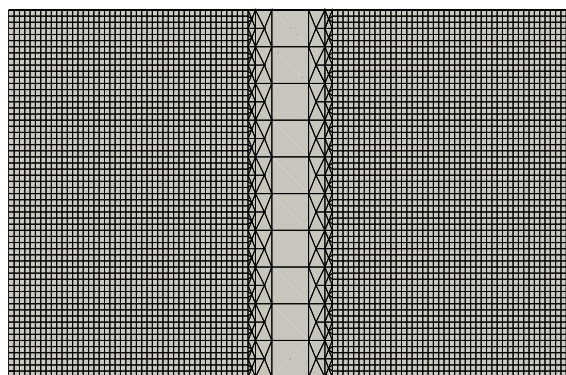
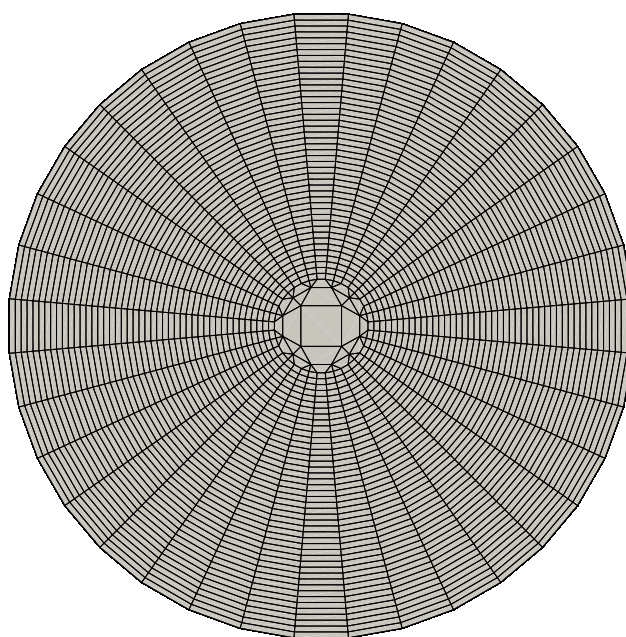


Figure 2 Shear rate-shear stress dependence. Points: measured values. Lines: best fits.



(a)



(b)

Figure 3 Example of the grids described in Table 4.

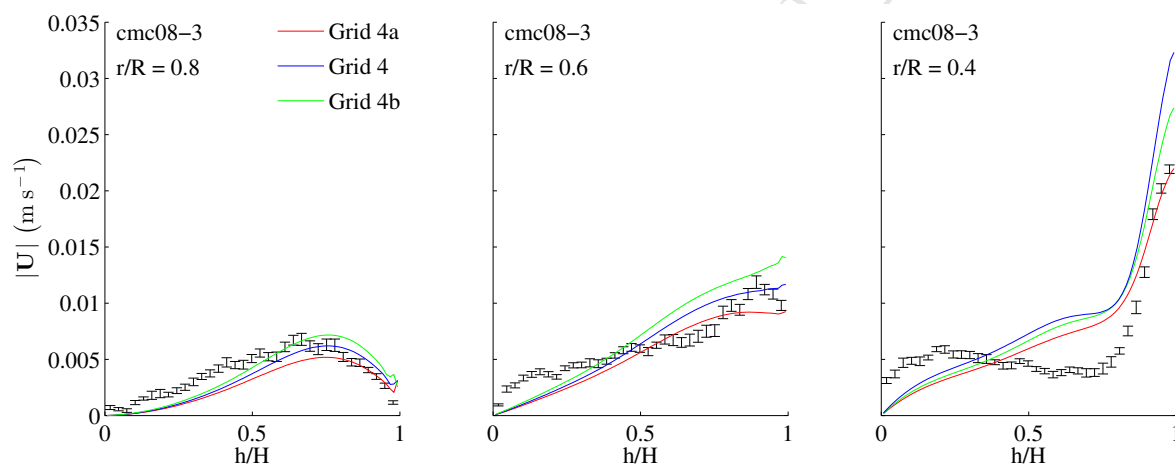


Figure 4 Preliminary series along a vertical axis against PIV outcome. Red: Grid 4a. Blue: Grid 4. Green: Grid 4b.

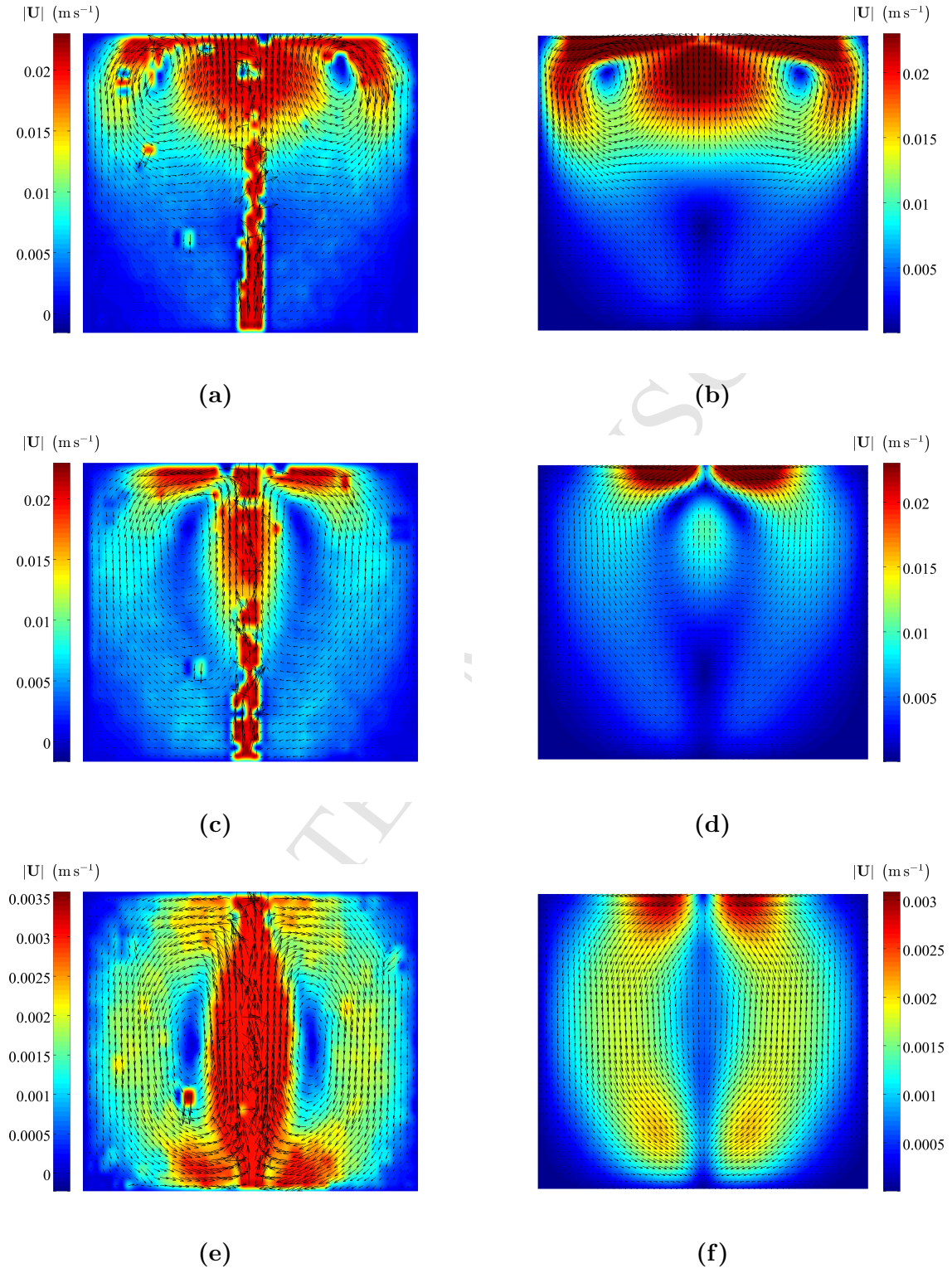


Figure 5 Projected velocity plots using the Grid 1. cfd02-2: (a): PIV outcome, (b): CFD simulation. cfd04-2: (c): PIV outcome, (d): CFD simulation. cfd08-2: (e): PIV outcome, (f): CFD simulation.

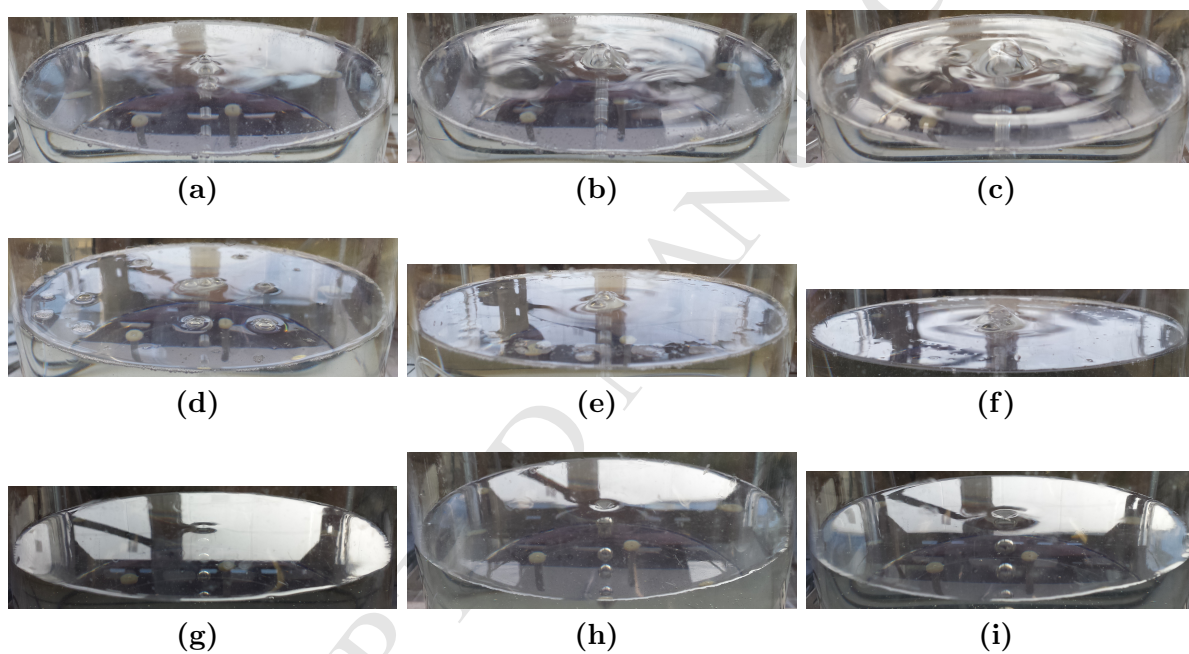


Figure 6 *Liquid-air interface.* (a): *cmc02-1.* (b): *cmc02-2.* (c): *cmc02-3.* (d): *cmc04-1.* (e): *cmc04-2.* (f): *cmc04-3.* (g): *cmc08-1.* (h): *cmc08-2.* (i): *cmc08-3.*

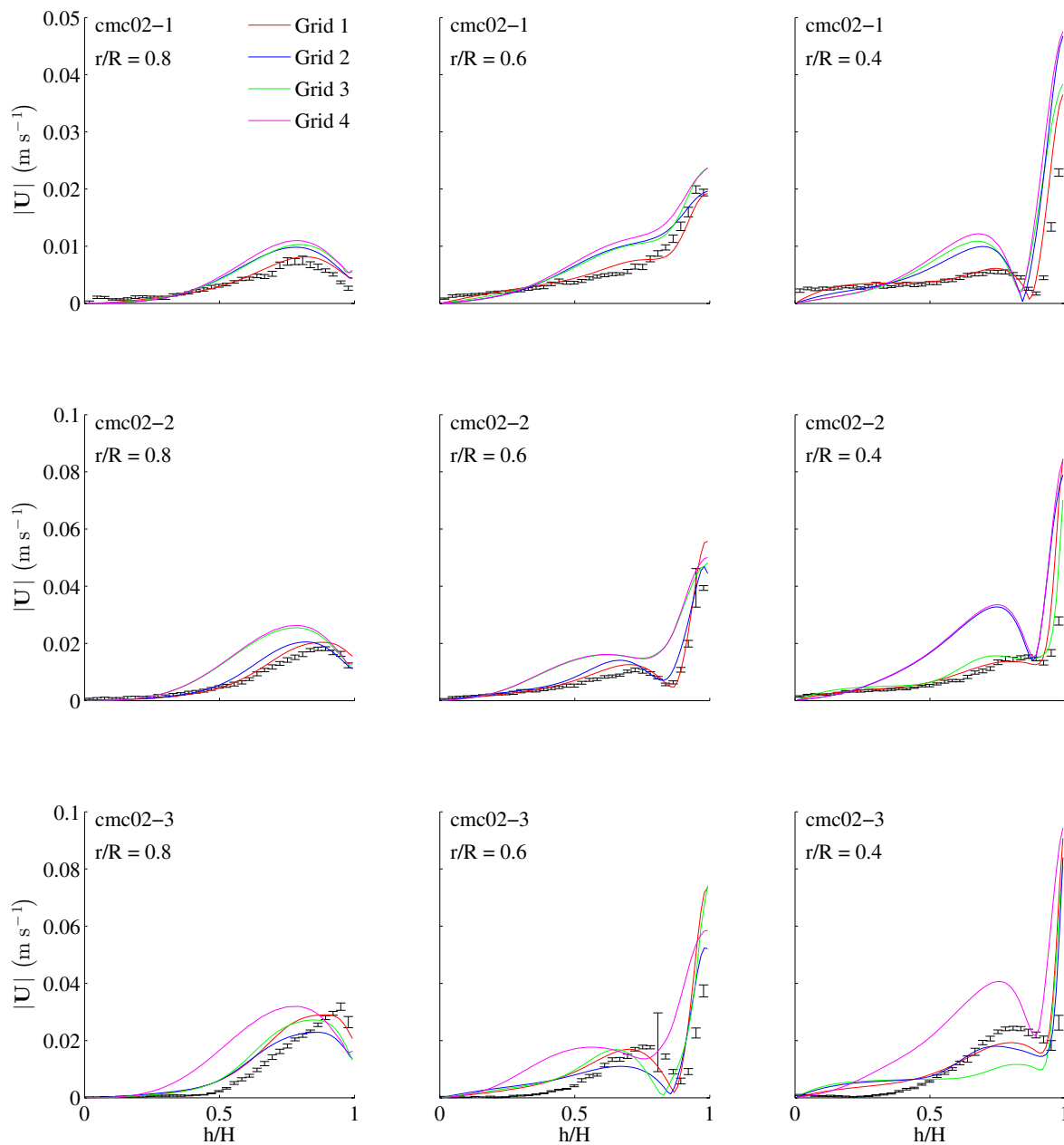


Figure 7 *CFD-simulated velocity magnitude along a vertical axis against PIV outcome. 2 g l^{-1} .*

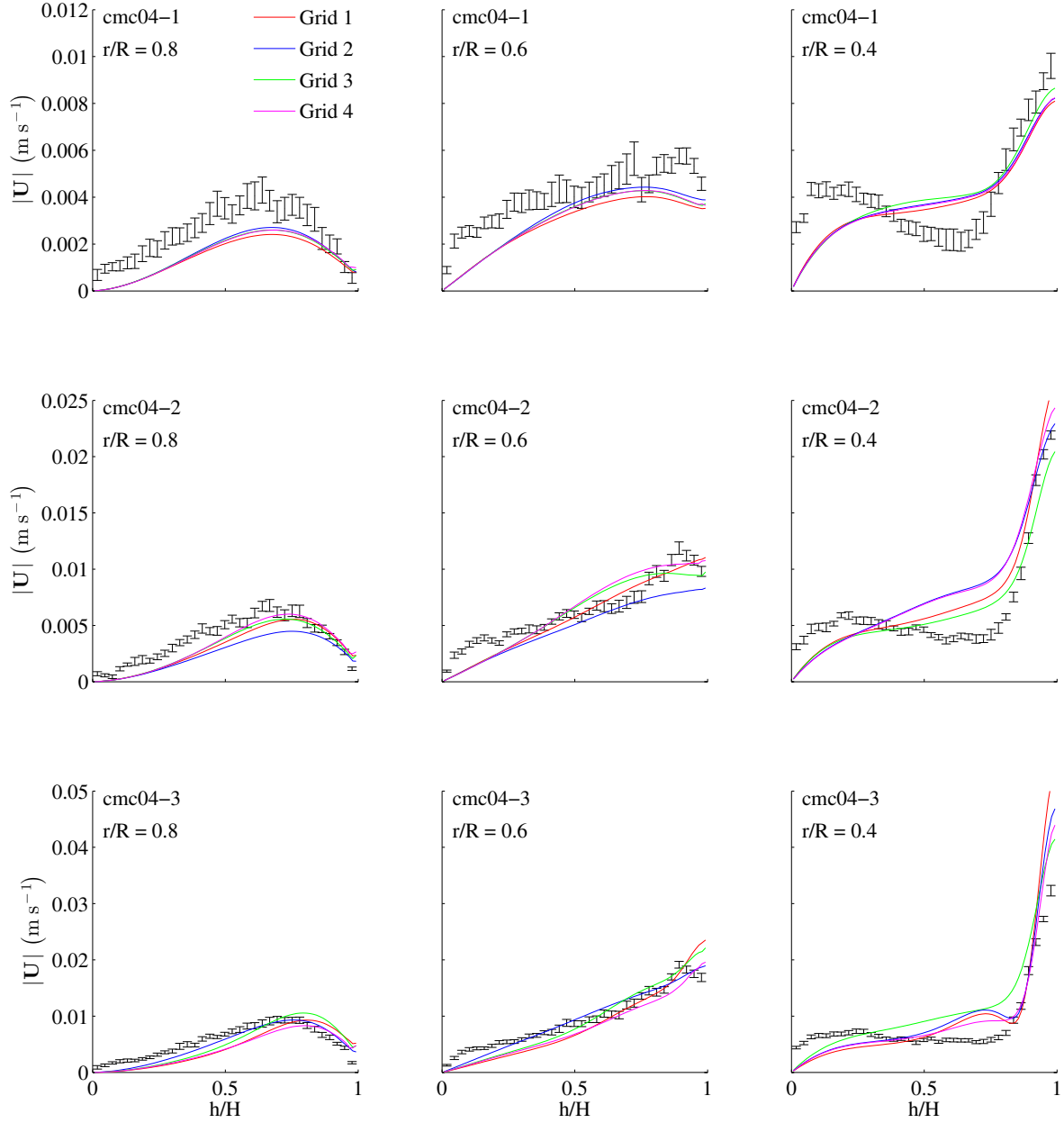


Figure 8 \nearrow CFD-simulated velocity magnitude along a vertical axis against PIV outcome. 4 g l^{-1} .

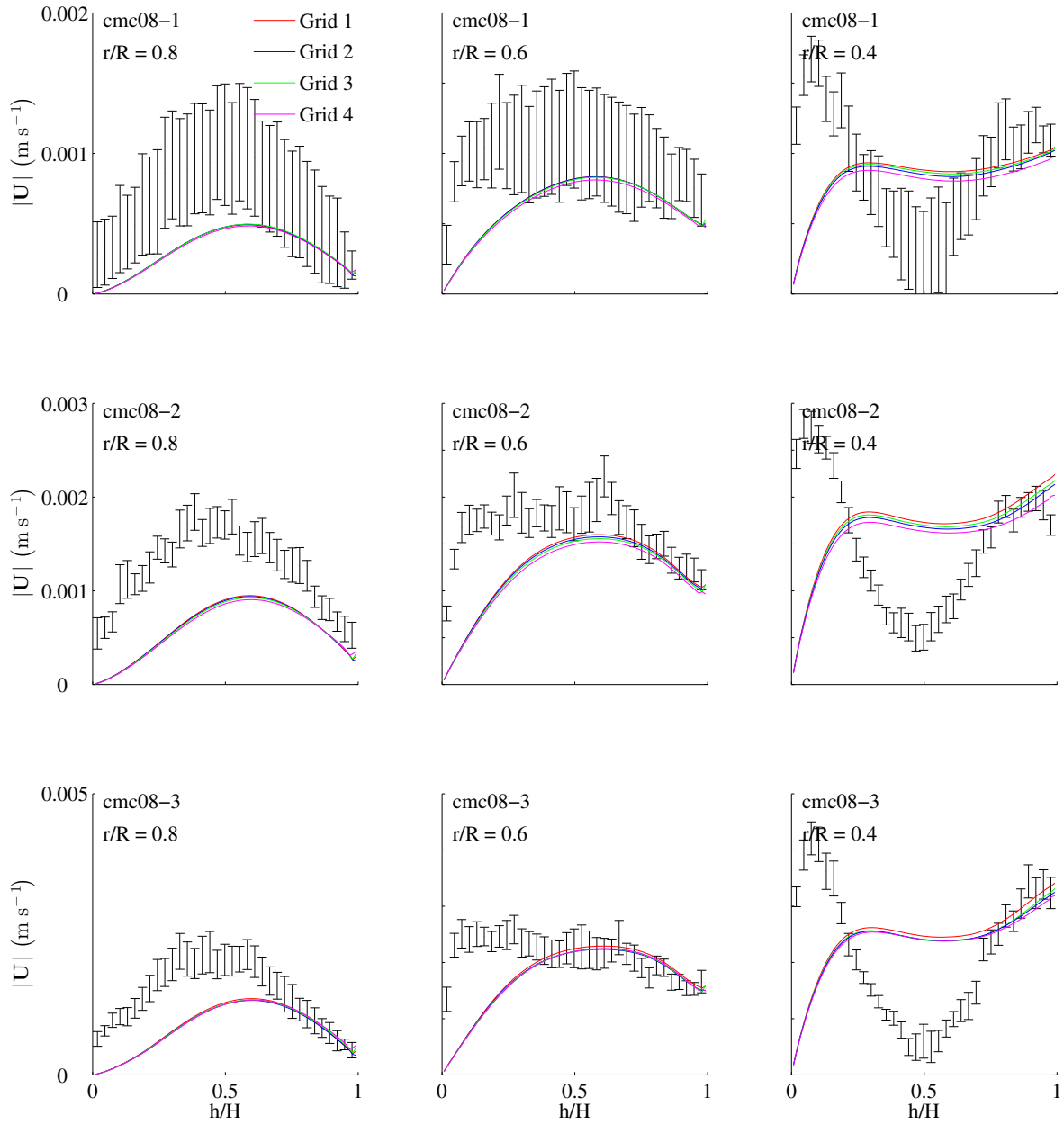


Figure 9 CFD-simulated velocity magnitude along a vertical axis against PIV outcome. 8 g l^{-1} .

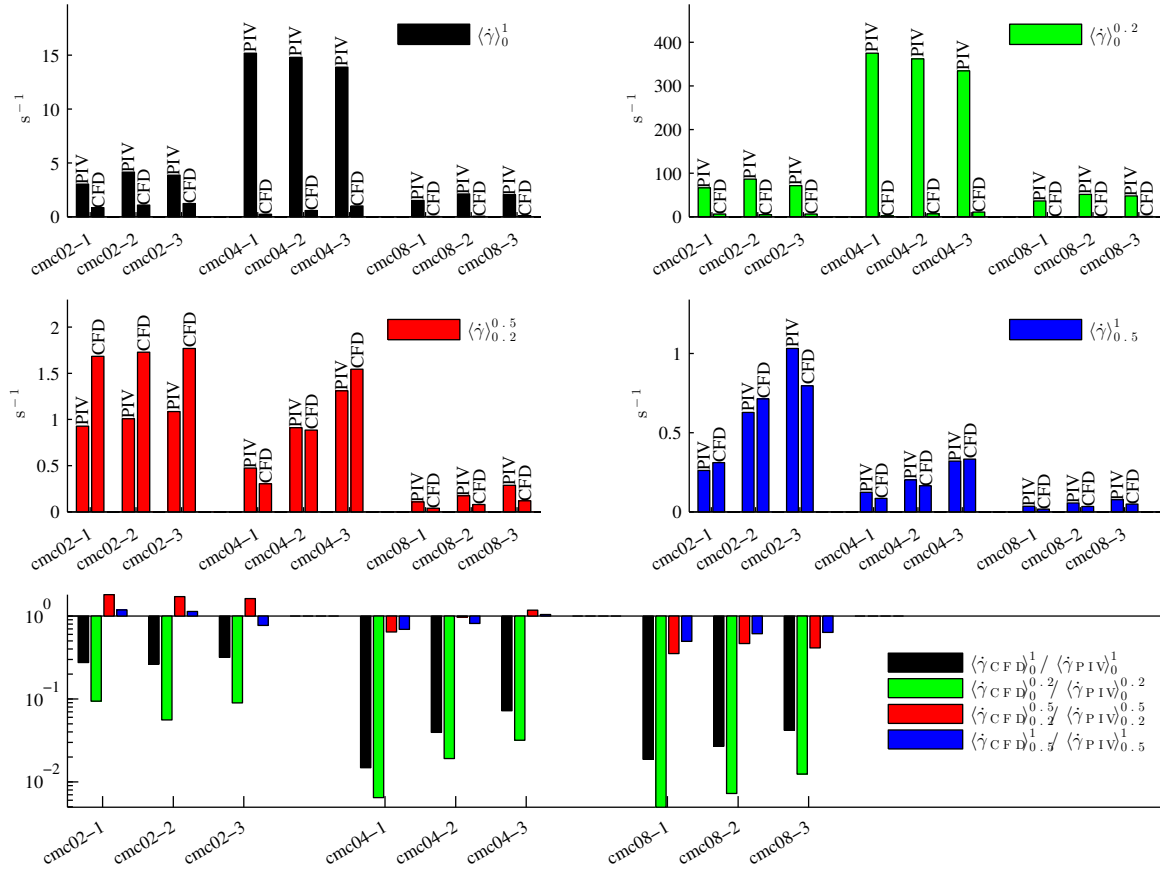


Figure 10 Average shear rate over different subdomains: comparison between experimental and simulated data. Below: ratio between simulated and experimental data.

743 **List of Tables**

744	1	Rheological properties of sludge at $T=35\text{ }^{\circ}\text{C}$ (from Achkari-Begdouri and	
745		Goodrich (1992)).	46
746	2	Fitted parameters for the shear rate-shear stress dependance.	47
747	3	High speed camera outcome.	48
748	4	Details of the grids.	49
749	5	Boundary and initial conditions.	50
750	6	GCI analysis. 2 g l^{-1}	51
751	7	GCI analysis. 4 g l^{-1}	52
752	8	GCI analysis. 8 g l^{-1}	53

Nomenclature

$\dot{\gamma}$	Shear rate, s^{-1}
Co	Courant number
Eo	Modified Eötvös number
Re_p	Bubble Reynolds number
μ	Power law viscosity, Pa s
ρ	Liquid phase density, kg m^{-3}
τ	Shear stress, Pa
\mathbf{g}	Acceleration of gravity, m s^{-1}
\mathbf{u}	Liquid phase velocity field, m s^{-1}
\mathbf{u}_p	Velocity of the p -th bubble, m s^{-1}
d_p	Diameter of the p -th bubble, m
K	Consistency coefficient, Pa s^n
m_p	Mass of the p -th bubble, kg
n	Power law index
p	Pressure, Pa
V_p	Volume of the p -th bubble, m^3
CFD	Computational Fluid Dynamics
CMC	Carboxymethyl cellulose
GCI	Grid Convergence Index
PIV	Particle Image Velocimetry

Table 1 Rheological properties of sludge at $T=35\text{ }^{\circ}\text{C}$ (from Achkari-Begdouri and Goodrich (1992)).

TS (%)	K (Pa s^n)	n (-)	$ \dot{\gamma} $ range (s^{-1})	μ_{\min} (Pa s)	μ_{\max} (Pa s)	Density (kg m^{-3})
2.5	0.042	0.710	226—702	0.006	0.008	1,000.36
5.4	0.192	0.562	50—702	0.01	0.03	1,000.78
7.5	0.525	0.533	11—399	0.03	0.17	1,001.00
9.1	1.052	0.467	11—156	0.07	0.29	1,001.31
12.1	5.885	0.367	3—149	0.25	2.93	1,001.73

Table 2 *Fitted parameters for the shear rate-shear stress dependance.*

Label (-)	Concentration (g l ⁻¹)	K (Pa s ^{n})	n (-)
cmc02-*	2	0.054	0.805
cmc04-*	4	0.209	0.730
cmc08-*	8	1.336	0.619

Table 3 *High speed camera outcome.*

Label (-)	Q (ml s ⁻¹)	d (mm)	Figures (-)
cmc02-1	2.05	7.01	7
cmc02-2	5.30	7.01	5a, 5b, 7
cmc02-3	8.63	7.01	7
cmc04-1	2.05	7.94	8
cmc04-2	5.30	7.94	5c, 5d, 8
cmc04-3	8.63	7.94	8
cmc08-1	2.05	11.0	9
cmc08-2	5.30	12.8	5e, 5f, 9
cmc08-3	8.63	13.8	9

Table 4 *Details of the grids.*

Grid Id.	Cells no.	Central cells size	Central cells no.	Cells over circle
1	2,348,787	9.19 mm	10	72
2	1,361,367	9.19 mm	10	60
3	230,410	9.19 mm	10	48
4a	121,240	7.66 mm	12	36
4	97,210	9.19 mm	10	36
4b	77,992	11.0 mm	8	36

Table 5 *Boundary and initial conditions.*

Place	Quantity	Condition
Top	p	Constant zero
	\mathbf{u}	Slip
	ε	Slip
	R_{ij}	Slip
Wall / bottom	p	Adjusted such that the velocity flux is zero
	\mathbf{u}	Constant zero
	ε	Wall function
	R_{ij}	Wall function

Table 6 *GCI analysis. 2 g l⁻¹.*

	cmc02-1	cmc02-2	cmc02-3
$\langle \dot{\gamma} \rangle_4$ (s ⁻¹)	0.9662	1.7051	1.9331
$\langle \dot{\gamma} \rangle_3$ (s ⁻¹)	0.8757	1.6717	1.4556
$\langle \dot{\gamma} \rangle_2$ (s ⁻¹)	0.8357	1.0916	1.2244
$\langle \dot{\gamma} \rangle_1$ (s ⁻¹)	0.6446	1.2838	1.5850
p_2	3.855	2.755	3.605
p_1	—	2.337	—
GCI ₂₄₃	6.360 10 ⁻²	2.065 10 ⁻²	2.252 10 ⁻¹
GCI ₂₃₂	6.799 10 ⁻³	1.616 10 ⁻¹	3.167 10 ⁻²
GCI ₁₃₂	—	2.222 10 ⁻¹	—
GCI ₁₂₁	—	3.536 10 ⁻¹	—
Asymp.2	0.954	0.025	0.841
Asymp.1	—	0.411	—

Table 7 *GCI analysis. 4 g l⁻¹.*

	cmc04-1	cmc04-2	cmc04-3
$\langle \dot{\gamma} \rangle_4$ (s ⁻¹)	0.2125	0.5358	0.8568
$\langle \dot{\gamma} \rangle_3$ (s ⁻¹)	0.2144	0.6393	0.8829
$\langle \dot{\gamma} \rangle_2$ (s ⁻¹)	0.2249	0.4586	0.9994
$\langle \dot{\gamma} \rangle_1$ (s ⁻¹)	0.2076	0.5866	1.3548
p_2	1.314	0.725	1.028
p_1	—	2.809	—
GCI ₂₄₃	2.397 10 ⁻²	8.729 10 ⁻¹	1.071 10 ⁻¹
GCI ₂₃₂	4.974 10 ⁻²	9.185 10 ⁻¹	1.739 10 ⁻¹
GCI ₁₃₂	—	1.152 10 ⁻¹	—
GCI ₁₂₁	—	4.091 10 ⁻¹	—
Asymp.2	0.221	0.619	0.335
Asymp.1	—	0.169	—

Table 8 *GCI analysis. 8 g l⁻¹.*

	cmc08-1	cmc08-2	cmc08-3
$\langle \dot{\gamma} \rangle_4$ (s ⁻¹)	0.0273	0.0549	0.0841
$\langle \dot{\gamma} \rangle_3$ (s ⁻¹)	0.0282	0.0570	0.0848
$\langle \dot{\gamma} \rangle_2$ (s ⁻¹)	0.0283	0.0573	0.0851
$\langle \dot{\gamma} \rangle_1$ (s ⁻¹)	0.0285	0.0582	0.0864
p_2	8.134	7.458	3.258
p_1	—	—	—
GCI ₂₄₃	4.272 10 ⁻³	6.124 10 ⁻³	6.089 10 ⁻³
GCI ₂₃₂	3.447 10 ⁻⁵	7.365 10 ⁻⁵	8.811 10 ⁻⁴
GCI ₁₃₂	—	—	—
GCI ₁₂₁	—	—	—
Asymp.2	1.003	1.005	1.004
Asymp.1	—	—	—

- A CFD model for gas mixing in anaerobic digestion is developed.
- We present the first Euler-Lagrange model for the scope.
- Motion arises by momentum transfer from bubbles to liquid phase.
- Lab-scale validation with PIV technique was carried out.
- The model reproduces well the experimental data.